PHYSICAL REVIEW C **94**, 025803 (2016)

Measurement of the $E_r^{\text{c.m.}} = 259$ keV resonance in the $^{14}\text{N}(p,\gamma)^{15}\text{O}$ reaction

S. Daigle,[*] K. J. Kelly, A. E. Champagne, M. Q. Buckner,[†] C. Iliadis, and C. Howard[‡]
University of North Carolina at Chapel Hill, Chapel Hill, North Carolina 27599-3255, USA
and Triangle Universities Nuclear Laboratory, Durham, North Carolina 27708-0308, USA
(Received 7 April 2016; published 22 August 2016)

The $^{14}\text{N}(p,\gamma)^{15}\text{O}$ reaction regulates the power generated by the CN cycle and thus impacts the structure and evolution of every star at some point in its life. The lowest positive-energy resonance in this reaction is located at $E_r^{\text{c.m.}} = 259$ keV, too high in energy to strongly influence quiescent stellar burning. However, the strength of this resonance is used as a cross-section normalization for lower-energy measurements of this reaction. We report on new measurements of the energy, strength, and γ-ray branching ratios for the 259-keV resonance, using different detection and data-analysis schemes. We have also reevaluated previous results, where possible. Our new recommended strength of $\omega\gamma = 12.6(3)$ meV is in agreement with the previous value of 13.1(6) meV, but is more precise and thus provides a more reliable normalization for low-energy (p,γ) measurements.

DOI: 10.1103/PhysRevC.94.025803

I. INTRODUCTION

At low stellar temperatures, the rate of energy generation in the CN cycle is regulated by the slowest reaction, $^{14}\text{N}(p,\gamma)^{15}\text{O}$. Recent measurements of this reaction [1–6] have shown that the reaction rate at low temperatures is about 40% lower than had previously been assumed [7], which has implications for stellar structure and evolution. For example, the ages of old globular clusters as determined from the luminosity at the main-sequence turnoff are found to be increased by about 0.7 Gy [8]. In addition, the predicted flux of solar neutrinos from the CNO cycle is reduced by about a factor of 2 (see, e.g. [8,9]), which has implications for experiments designed to measure these neutrinos [10–15], as well as for the potential interpretation of these measurements in terms of the solar metallicity [16].

The previous measurements of the $^{14}\text{N}(p,\gamma)^{15}\text{O}$ reaction fall into two main classes: measurements of astrophysical S factors for individual decay branches [1–3,6,7], and calorimetric measurements of the total S factor [4,5]. The latter extend down to energies corresponding to nucleosynthesis in AGB stars, but it has not been possible to extrapolate those measurements to the lower energies characteristic of red-giant or main-sequence stars. The former measurements have larger systematic uncertainties, but can be extrapolated to lower energies using R-matrix techniques. The S factors reported in the newer measurements [1–3,6] were measured relative to the strength of the $E_r^{\text{c.m.}} = 259$-keV resonance in the $^{14}\text{N}(p,\gamma)^{15}\text{O}$ reaction, which corresponds to an excited state at $E_x = 7556.5(4)$ keV [17] in ^{15}O (the S factors in Ref. [7] were obtained relative to a standard cross section, which depended in part on this resonance strength). A recent review of solar-fusion reactions by Adelberger *et al.* [18] presented revised R-matrix fits of the combined data of Refs. [2,3,6,7], each of which was separately normalized to a recommended resonance strength of $\omega\gamma_{259} = 13.1(6)$ meV for the 259-keV resonance. This value was derived from a weighted average of previous results [2,3,5,19]. The quoted uncertainty includes a common systematic uncertainty in the stopping power of protons in nitrogen derived from SRIM calculations [20]. However, the measurement of Becker *et al.* [19] was carried out in inverse kinematics and used stopping powers from Northcliffe and Schilling [21], thus this result must be handled differently than the others. In addition, the original resonance strengths depended on the branching ratio for the particular γ-ray transition measured and these same branching ratios come into play when experimental yields are converted into S factors for individual transitions. The branching ratios reported in Refs. [2,3] were each measured using a large-volume high-purity germanium (HPGe) detector at a distance of 20 cm from the target, chosen to reduce coincidence summing to a negligible level. While this distance was indeed sufficient to minimize the effect of summing for the stronger transitions, the comparatively weak transition to the ground state of ^{15}O still had a contribution from coincidence summing on the order of 8% in Ref. [2] and most likely a similar amount in Ref. [3]. Although the ground-state transition is a weak branch ($\sim$1.5%) in the decay of the 259-keV resonance, it is the second largest contributor to the low-energy $^{14}\text{N}(p,\gamma)^{15}\text{O}$ S factor. Subsequent measurements [6] with an HPGe clover detector did succeed in reducing summing to a negligible level for the strong transitions and to a 2% level for the ground-state transition.

As noted in Ref. [18], the total S factor as a function of energy as derived from the new R-matrix fits is 8% higher on average than the two measurements of the total S factor [4,5]. This disagreement becomes worse if the R-matrix fits of Artemov *et al.* [22] are used instead, but it should be noted that they have not renormalized the capture data and also recommend a much larger overall uncertainty (17% vs 7% in Ref. [18]). On the other hand, the recommended S factor

[*]Current address: NASA Postdoctoral Program, NASA Marshall Space Flight Center, Huntsville, AL 35812, USA; stephen.daigle@nasa.gov
[†]Current address: Lawrence Livermore National Laboratory, Livermore, CA 94550-9234, USA.
[‡]Current address: Nordion, 447 March Rd, Kanata, ON K2K 1X8, Canada.

of Adelberger *et al.* [18] is in excellent agreement with a coupled-channels analysis [23] of a more restricted data set (taken from Refs. [2,3]). The uncertainty in the value for $S(0)$ recommended by Adelberger *et al.* has roughly equal contributions of approximately 5% from the systematics of the R-matrix fits and from $\omega\gamma_{259}$. Thus, an improved value for $\omega\gamma_{259}$ would make the R-matrix fits the dominant source of uncertainty and there is reason to expect that these can be improved upon. For example, a multichannel R-matrix fit combining capture and elastic-scattering data yields an improved determination of the S factor for the ground-state transition [24].

The 259-keV resonance plays a central role in determining the low-energy S-factor from $^{14}\mathrm{N}(p,\gamma)^{15}\mathrm{O}$ measurements, and thus an improved measurement of the resonance strength is called for. In the present work, we report on new measurements of $\omega\gamma_{259}$ using complementary techniques with different systematic uncertainties, as well as a reevaluation of existing results. We also present new branching ratios for the decay of this resonance as well as the resonance energy and excitation energies for the states populated by the major decay branches. Our recommended resonance strength, $\omega\gamma_{259} = 12.6(3)$ meV, is about 3.8% lower than the recommended [18] value and is also more precise. At this level of uncertainty, the overall uncertainty in $S(0)$ would be dominated by uncertainties associated with the R-matrix fits.

II. EXPERIMENTAL PROCEDURE

A. Accelerators

We measured the $^{14}\mathrm{N}(p,\gamma)^{15}\mathrm{O}$ reaction at the Laboratory for Experimental Nuclear Astrophysics (LENA), located at the Triangle Universities Nuclear Laboratory. A 1 MV JN Van de Graaff accelerator supplied proton beams of up to 100 μA on target in the energy range of $E_p^{\mathrm{lab}} = 272$–310 keV. The bombarding energy was calibrated to better than ± 1 keV using well-known resonances in the $^{18}\mathrm{O}(p,\gamma)^{19}\mathrm{F}$, $^{26}\mathrm{Mg}(p,\gamma)^{27}\mathrm{Al}$, and $^{27}\mathrm{Al}(p,\gamma)^{28}\mathrm{Si}$ reactions. The energy spread of the beam was typically 1–2 keV. The beam entered the target chamber through a liquid-nitrogen-cooled copper tube that was biased to -300 V in order to suppress the emission of secondary electrons from the target and the beam collimator. The target was directly water cooled using deionized water and, with the target chamber, formed a Faraday cup for charge integration. We also performed Rutherford backscattering measurements using a 2.0-MeV $^4\mathrm{He}^+$ beam provided by the Triangle Universities Nuclear Laboratory FN tandem accelerator.

B. Targets

The nitrogen targets used in our measurements were prepared by implanting $^{14}\mathrm{N}_2^+$ ions into 0.35(5)-mm-thick tantalum backings (99.95% metals-basis purity). Prior to implantation, the backings were wet-etched in an acid solution [25] to remove surface impurities, then rinsed in 200-proof ethanol and resistively heated inside a high-vacuum ($<10^{-7}$ Torr), oil-free evaporator system at LENA. The target backings were later stored in an evacuated polycarbonate target box to inhibit the formation of an oxide layer on the surface of the tantalum. The prepared tantalum backings were implanted with nitrogen using an Eaton NV-3206 ion implanter at the University of North Carolina, at an energy of 40 keV, with average beam currents of 30–40 μA and incident doses of 30 $\mu\mathrm{g/cm}^2$. These implantation parameters produced targets of about 10-keV thickness at $E_r^{\mathrm{c.m.}} = 259$ keV. To ensure uniform implantation profiles, the N_2^+ beam was rastered across the surface of the tantalum backing, and a beam scanner was utilized to monitor the beam profile during implantation. The target chamber was maintained at pressures below 5×10^{-7} Torr and a liquid-nitrogen-cooled copper shroud positioned before the target prevented carbon and other contaminants from plating onto the surface of the tantalum backing.

The target stoichiometry was determined via Rutherford backscattering spectrometry (RBS). This utilized a LabVIEW-controlled, semiautomatic target system [26] that allowed for multiple targets and precise positioning with respect to the incident α-beam, which was collimated to 3 mm $\times$ 3 mm. The target wheel was inclined at an angle of 22.5° with respect to the beam. Backscattered α particles were detected using a Si(SB) detector, mounted approximately 24.4 cm away from the target wheel at an angle of 160° with respect to the beam direction. A 1.0 mm (horiz.) $\times$ 9. mm (vert.) aperture was mounted in front of the detector to limit the count rate of backscattered α particles and to precisely define the scattering angle.

RBS spectra were taken of one tantalum backing, two unused targets, and five targets that had undergone proton bombardment at LENA (with accumulated charge ranging from 5.0 to 8.7 C). Each target was profiled near the center and near the edge of the implanted region. The energy calibration of the backscattered α particles was determined from the high-energy edge of RBS spectra collected from gold and aluminum samples as well as from the tantalum backing. Each spectrum was subsequently fit using the simulation code SIMNRA [27], with SRIM [20] stopping powers. This involved dividing the implantation profile into layers, and the nitrogen concentration and thickness of each layer were varied to produce the best fit to the data. Five layers (including one of pure tantalum) were sufficient to produce fits with reduced χ^2 values of 1.1–1.4. An example of a fit is shown in Fig. 1.

All of the targets showed the same general features, namely a thin surface layer of relatively low nitrogen concentration, followed by a region of saturation density that then tailed into the tantalum backing. As will be discussed in more detail below, only the stoichiometry of the high-concentration region is needed to extract the resonance strength from the thick-target yield. The statistical uncertainties in the extracted concentrations include contributions from uncertainties in the energy calibration (2.2%), the quality of the fit (2.5%), and the sensitivity of the fit to the starting guess for the concentration profile (1%), all of which we take to be uncorrelated. These percentages are normal approximations to estimated probability densities and give rise to an overall statistical uncertainty of 3.5%. In addition, there is a systematic uncertainty in the nitrogen concentration that is associated with the uncertainties in the stopping powers for nitrogen and tantalum. The concentration of nitrogen is $(1 + \mathrm{Ta/N})^{-1}$ and the systematic uncertainty in Ta/N is approximately

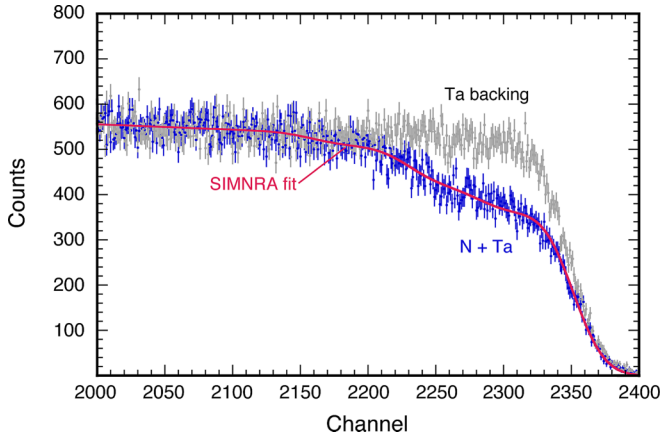

FIG. 1. RBS spectra from an implanted target (blue) and a tantalum backing (grey). The SIMNRA [27] fit is shown in red.

proportional to the uncertainty in the ratio of stopping powers, $\epsilon(\text{N})/\epsilon(\text{Ta})$ (see, e.g., Eq. 1 of Ref. [28]). For energies near $E_\alpha = 2$ MeV, we estimate uncertainties of 2.8% and 1.6%, respectively for $\epsilon(\text{N})$ and $\epsilon(\text{Ta})$. Consequently, the Ta/N ratio has a systematic uncertainty of 3.2%, which results in a systematic uncertainty of 1.3% in the nitrogen concentration. With the exception of the target with the highest accumulated charge (8.7 C), the used targets had nitrogen concentrations equivalent to those of the two fresh targets and, additionally, the concentration was found to be uniform across each target to better than 10%, as shown in Fig. 2. According to Peirce's criterion [29], none of these points would be identified as an outlier, which implies that actual differences in nitrogen concentrations are small as compared to the uncertainties. An average of these data yields a concentration of ^{14}N of $0.600 \pm 0.010(\text{stat}) \pm 0.008(\text{sys})$ (all uncertainties in this paper are quoted at the 1σ level). Note that the statistical

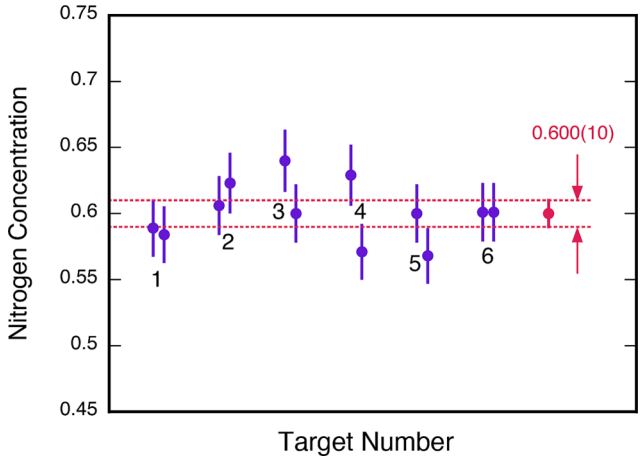

FIG. 2. Relative concentration of ^{14}N in the region of saturation density. Each pair of closely spaced points corresponds to a different target, with two measurements at different locations on the same target. Note that only statistical uncertainties are shown. The average is denoted by the red point and the uncertainty calculated via bootstrapping is indicated by the dashed lines.

uncertainty is 50% larger than what would be determined using the standard expression for the uncertainty of an average, $\sigma_i/\sqrt{n}$, where σ_i is the standard deviation in an individual measurement and n is the number of measurements. However, since the uncertainties in each measurement are estimated from normal approximations of the individual uncertainties, this expression (and the corresponding one for a weighted average) can underestimate the uncertainty in the average. As a result, we have chosen to calculate the standard deviation in the average via a bootstrap method (see, e.g., [30]), using the Visual Averaging Library tool [31]. Combining statistical and systematic uncertainties, the relative concentration of ^{14}N is 0.600(13), which is in excellent agreement with a previous measurement of 0.61(2) [28]. The corresponding ratio of tantalum to nitrogen is 0.667(21) (note that the uncertainties in the nitrogen and tantalum concentrations are correlated and do not simply add).

C. Detectors

Two different detector systems were used for our measurements of the 259-keV resonance. The first was a standard HPGe detector while the second was an APEX trigger detector [32], an annulus of position-sensitive NaI(Tl) detectors originally constructed for the ATLAS Positron Experiment (APEX) [33] and on loan from Argonne National Laboratory. Each detector had specific advantages and disadvantages for the measurements described here. The HPGe detector has comparatively high resolving power, but its relatively low efficiency necessitated placing the detector in close proximity to the target. Thus, coincidence summing could not be ignored. In contrast, the geometry and position sensitivity of the APEX detector significantly reduced coincidence summing, but at the expense of poor energy resolution (as compared to HPGe). These limitations were overcome using techniques that we will describe in Sec. III B. The complementary features of these detectors provided an important check on possible sources of systematic uncertainty. Each detector is described in more detail below.

1. HPGe

The HPGe detector is coaxial with a diameter of 89.0 ± 0.5 mm and a length of 91.6 ± 1.0 mm, resulting in 135% relative efficiency. The critical dimensions were determined from a CT scan [34]. It was centered axially on the beam line at 0° with respect to the target chamber at distances ranging from 1.6 to 21.6 cm, measured from the front of the target to the front of the crystal. The HPGe and target chamber were surrounded by an annulus of NaI(Tl) scintillators, which were not used for these measurements. The HPGe and NaI(Tl) detectors were then surrounded on all sides by a 12.7 mm thickness of lead, which was in turn encased on all sides (except for the bottom) by 50-mm-thick plastic scintillating paddles [35], used as a veto for cosmic-ray induced muons.

Efficiency measurements for γ-ray energies below 3 MeV were made by using radioactive sources of ^{22}Na, ^{54}Mn, ^{56}Co, ^{60}Co, and ^{137}Cs. For γ-ray energies above 3 MeV, the nuclear reactions $^{18}\text{O}(p,\gamma)^{19}\text{F}$, $^{23}\text{Na}(p,\gamma)^{24}\text{Mg}$, and $^{27}\text{Al}(p,\gamma)^{28}\text{Si}$ were measured. The data for all sources and reactions emitting

more than one γ ray were corrected for coincidence summing. To remove any reliance on knowledge of the activities of the various sources, the *sum-peak method* [36], utilizing ^{60}Co, was used to obtain an absolute efficiency to which the other source and reaction data could be normalized. Extensive Monte Carlo simulations with GEANT version 4.9.6 [37] have been performed [38] and there is excellent agreement between measurements and simulations. Finally, the energy calibration of the HPGe detector was measured using well-resolved background lines from ^{40}K, ^{208}Tl, ^{212,214}Bi, and ^{228}Ac.

2. APEX

The APEX detector consists of 24 position-sensitive NaI(Tl) detectors arranged in an annulus. Each bar is trapezoidal in cross section with dimensions $55.0 \times 6.0 \times 5.5/7.0$ cm^3 (L × H × W). The NaI(Tl) segments are held by two stainless steel rings and the entire array is surrounded by a 1.9-cm-thick cylindrical lead shield resting inside an aluminum cradle, which was centered on the target chamber. Each crystal is encapsulated by a 0.4 mm thick stainless steel container with quartz windows, 4.4 cm in diameter and 1.1 cm thick, permanently fixed at either end. GEANT4 simulations were carried out and included the target, target chamber, copper shroud, surrounding beam pipe, the NaI(Tl) crystals in their stainless steel containers, the quartz windows, and the lead shield wrapped inside the aluminum detector cradle, as shown in Fig. 3.

Each NaI(Tl) bar has a photomultiplier tube (PMT) coupled to either end. The original Hamamatsu R2490 tubes were chosen specifically for their performance in a strong magnetic field, but also produced asymmetric peak shapes. To improve this, we replaced these tubes with 32 Hamamatsu R580 tubes and 16 Photonis XP2012B tubes. A critical feature of the APEX detector for our purposes is its ability to read out both the position and energy of γ-ray interactions in each scintillator. As described in Ref. [32], the surfaces of each crystal were ground to produce an exponential attenuation of scintillation light along the length of the crystal. As a result, the position can be reconstructed by comparing the relative pulse

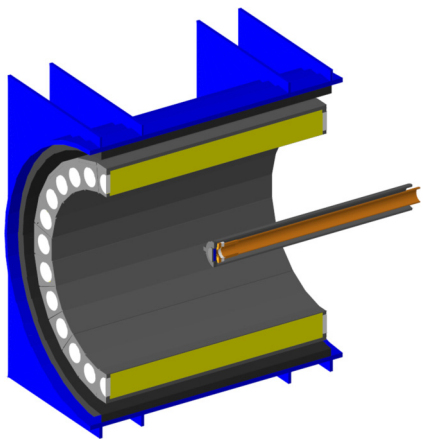

FIG. 3. Cutaway view of the GEANT4 geometry used in the Monte Carlo simulation of the APEX detector. The beam enters the target chamber from the right.

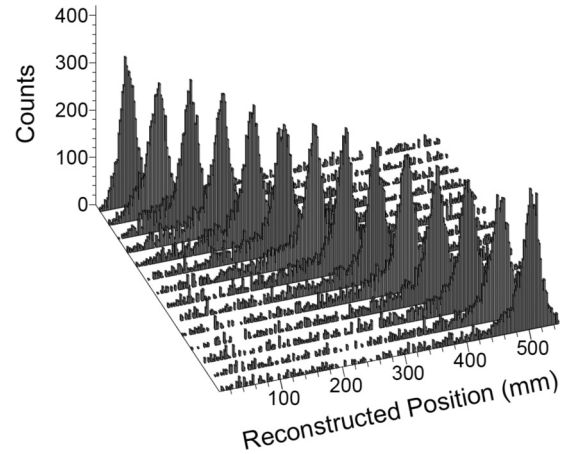

FIG. 4. Reconstructed positions of 1333-keV γ rays from a ^{60}Co source after position calibration. The compilation of histograms are for one NaI(Tl) segment as the source was moved in 3.5 cm increments along the length of the detector.

heights from each PMT. The reconstructed position is given by

$$X = \frac{1}{2\mu} \ln \frac{A_2}{A_1}, \tag{1}$$

where A_1 and A_2 are the pulse amplitudes from PMT 1 and 2 respectively. The reconstructed energy is proportional to the square root of the product of the signal pulses,

$$E_\gamma \propto \sqrt{A_1 A_2}. \tag{2}$$

The reconstructed energy was found to depend on the position and so a position-dependent correction was applied in software for the energy measured in each NaI(Tl) segment.

The position calibration of each detector was performed by moving a collimated, 0.25-μCi ^{60}Co source along the symmetry axis of the array. Each detector bar was subdivided into 16 position intervals by placing software gates in the reconstructed position histograms. The length of each pixel was chosen to be comparable to the measured position resolution of 3.5 cm FWHM. A series of reconstructed position histograms for one APEX segment is shown in Fig. 4.

The energy calibration of the APEX detector was accomplished in two steps, the first was to remove the position dependence of the reconstructed energy using the collimated ^{60}Co data. The second step was to expand the calibration to higher γ-ray energies using the 1460.8-keV and 2614.5-keV lines from ^{40}K and ^{208}Tl and literature [17] values for γ rays emitted by the 259-keV resonance in the ^{14}N$(p,\gamma)^{15}$O reaction. This included the primary and secondary γ-ray transitions, single-escape peaks, and the characteristic 511-keV positron annihilation radiation from the β^+ decay of ^{15}O. A typical energy resolution of 14% was measured using the $E_\gamma = 662$ keV line from the decay of ^{137}Cs.

III. EXPERIMENTAL RESULTS

A. Excitation and resonance energies

The levels populated in the γ-ray decay of the 259-keV resonance are illustrated in Fig. 5. Excitation energies were

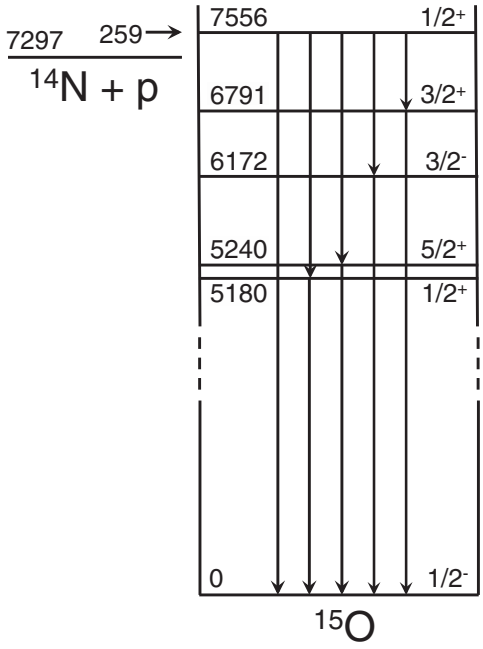

FIG. 5. Levels in ^{15}O populated in the γ-ray decay of the 259-keV resonance. Energies (in keV) are from Table I and Ref. [17].

extracted from ^{14}N$(p,\gamma)^{15}$O data collected at $E_p^{\text{lab}} = 284$ keV, using the HPGe detector. The detector was positioned at 1.62 cm (near) and 21.62 cm (far) from the target (measured from the target to the front face of the crystal), the farther distance was intended to minimize Doppler broadening. The spectrum collected in the near position is shown in Fig. 6. Peak positions were determined using the RADWARE package [39].

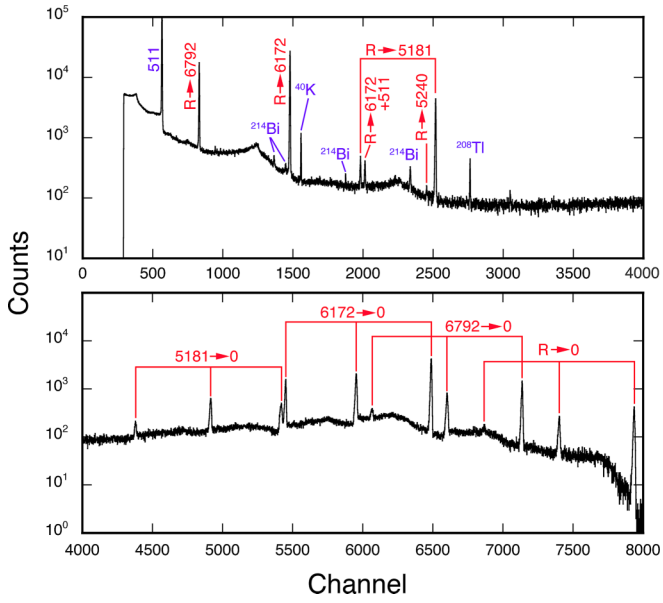

FIG. 6. Spectrum of the ^{14}N$(p,\gamma)^{15}$O reaction taken at $E_p^{\text{lab}} = 284$ keV with the HPGe detector. Gamma rays associated with the decay of the 259-keV resonance are labeled in red, background lines are denoted in purple.

The centroids of the γ-ray peaks are Doppler shifted, as described (relativistically) by

$$E_\gamma^{\text{obs}} = E_\gamma^0 \frac{\sqrt{1-\beta(t)^2}}{1-\beta(t)Q_1\cos\theta}, \quad (3)$$

where E_γ^{obs} is the observed energy, E_γ^0 is the unshifted energy, $\beta(t)$ is the recoil velocity (in units of c) and Q_1 is an angular attenuation coefficient, which corrects for the angular acceptance of the detector. This latter factor was calculated using GEANT4. The time-dependent recoil velocity can be written as $\beta(0)F(\tau)$, where $\beta(0)$ is the initial recoil velocity and $F(\tau)$ accounts for the slowing down of the recoil in the target over the mean lifetime. Because the short lifetime of the 259-keV resonance (0.00066 fs [17]), the Doppler shift is not attenuated, i.e., $\beta(t) = \beta(0)$. However, this is not necessarily the case for the secondary transitions. For example, lifetimes of 8.2(10) fs [17], 9.7(13) fs [40], and 8.4(10) fs [41] are reported for the 5181-keV state, but the lifetimes of the 6172- and 6792-keV states are quite uncertain [1,40–43]. Therefore, the excitation energies of the excited states populated in the decay of the 259-keV resonance were calculated from the excitation energy of the resonance and the energies of the primary transitions. The resulting excitation energies are listed in Table I. Note that in our list of previous results we have not included those of Ref. [1] because they appear to have been superceded in Ref. [3].

The uncertainties in our energies include contributions from the energy calibration and peak position (~0.3 keV), and smaller contributions from the Q_1 coefficient (3%), and β (~0.2%, from the energy calibration of the accelerator). There is excellent agreement between the present results and those of Refs. [3,17,44]. Thus, our adopted values are weighted averages (with uncertainties calculated via bootstrapping, as discussed previously), with the following caveats: The energies listed in Ref. [17] for the 5181-, 6172-, and 6792-keV states appear to be averages of several lower-precision results and thus were not included in our adopted energies. For the resonance ($E_x = 7556$ keV), the entry in Ref. [17] appears to originate from earlier measurements of the resonance energy, $E_r^{\text{lab}} = 278.1(4)$ keV. When combined with the Q value for the ^{14}N$(p,\gamma)^{15}$O reaction, $Q = 7296.78(49)$ keV (derived from

TABLE I. Summary of excitation energies (in keV).

Ref. [17]	Ref. [3]	Ref. [44]	This study		Adopted[a]
			Near	Far	
5183(1)	5180.8(3)		5179.7(6)	5180.5(4)	5180.4(3)
5240.9(3)			5239.8(10)		5240.4(6)[b]
6176.3(17)	6172.3(2)		6171.4(6)	6171.9(4)	6171.9(4)
6793.1(17)	6791.7(2)		6791.1(6)	6791.4(4)	6791.4(3)
7556.2(6)[c]	7556.4(6)	7555.7(55)[d]	7555.9(6)	7556.4(4)	7556.2(5)[e]

[a]Weighted average of Refs. [3,44] and present results, except where noted.
[b]Weighted average of Ref. [17] and this study.
[c]Corrected as described in text.
[d]Calculated from $E_p^{\text{lab}} = 277.60(27)$ keV and $Q = 7296.78(49)$ keV.
[e]Weighted average of all results.

TABLE II. Summary of resonance energies (center-of-mass frame, in keV).

Ref. [17]	Ref. [3]	Ref. [44]	This study		Adopted
			Near	Far	
259.4(4)	259.4(3)	258.95(25)	259.1(7)[a]	259.6(6)[a]	259.3(3)

[a]Calculated from $E_x - Q$.

the 2012 mass table [45]), we obtain $E_x = 7556.2(6)$ keV rather than the tabulated value of $E_x = 7556.5(4)$ keV. Consequently, we have used the former value in the weighted average.

The resonance energy can be measured directly from the 50% point of the (p,γ) yield curve [3,17,44]. However, the surface layer of an implanted target can shift this energy by about 1 keV (for our targets). Thus, we have calculated our value for $E_r^{\text{c.m.}}$ from $E_x - Q$. These energies are listed in Table II. Our recommended value is $E_r^{\text{c.m.}} = 259.3(3)$ keV.

B. Branching ratios

1. *HPGe measurements*

Gamma-ray branching ratios were measured using the HPGe detector, which was positioned at distances of 1.62, 6.62, 11.62, and 21.62 cm from the target to the detector crystal. These distances were chosen in order to probe the sensitivity of our results to varying levels of coincidence summing. For example, at a distance of 1.62 cm, about 76% of the yield of the ground-state transition arises from coincidence summing, which drops to about 8% at 21.62 cm. Although these spectra could be analyzed by traditional means, i.e., by integrating full-energy peaks and applying summing corrections, the net yield for the ground-state transition at close detector distances would necessitate subtracting two large numbers, which would compromise precision. Therefore, we have employed a fitting technique in which templates of the various components of the spectrum are varied independently in order to produce a fit to a region of the spectrum. The TFractionFitter [46] class of ROOT [47] was used to perform a maximum-likelihood fit in the energy range between 400 and 7600 keV. Applications of this technique are described in [48–50] and an identical approach is used here. Briefly, templates of the individual $^{14}\text{N}(p,\gamma)^{15}\text{O}$ transitions were constructed in GEANT4 and combined with a background template taken from measured background spectra and normalized to the total run times. Templates for all previously-observed transitions were simulated. The only possible decay that was ignored was an $M3$ transition to the 7276-keV state, which was excluded on the basis of γ-ray multipolarity. Those for γ cascades included the angular correlations between successive γ rays, which were calculated from the known [17] multipolarities and mixing ratios. A Gaussian smearing function was applied to the GEANT4 output to replicate the energy resolution of the HPGe detector. Using the notation of Ref. [49], the

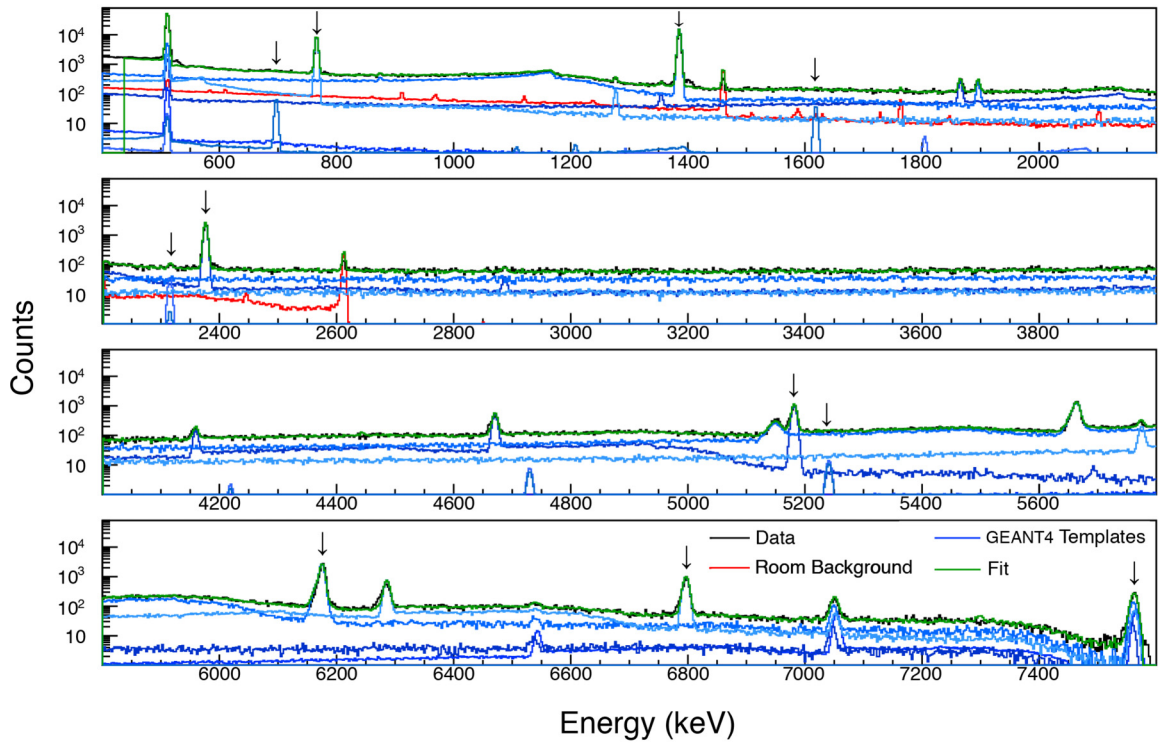

FIG. 7. The result of the best fit, shown in green, to HPGe data for the 259-keV resonance in the $^{14}\text{N}(p,\gamma)^{15}\text{O}$ reaction, shown in black, as derived using the TFractionFitter [46] class of ROOT [47] as described in the text and in Refs. [48,49]. Note that the data are not easily distinguished from the fit. Full-energy peaks for primary and secondary transitions are indicated by arrows and the corresponding templates are also shown in light and dark blue. The room-background spectrum is shown in red.

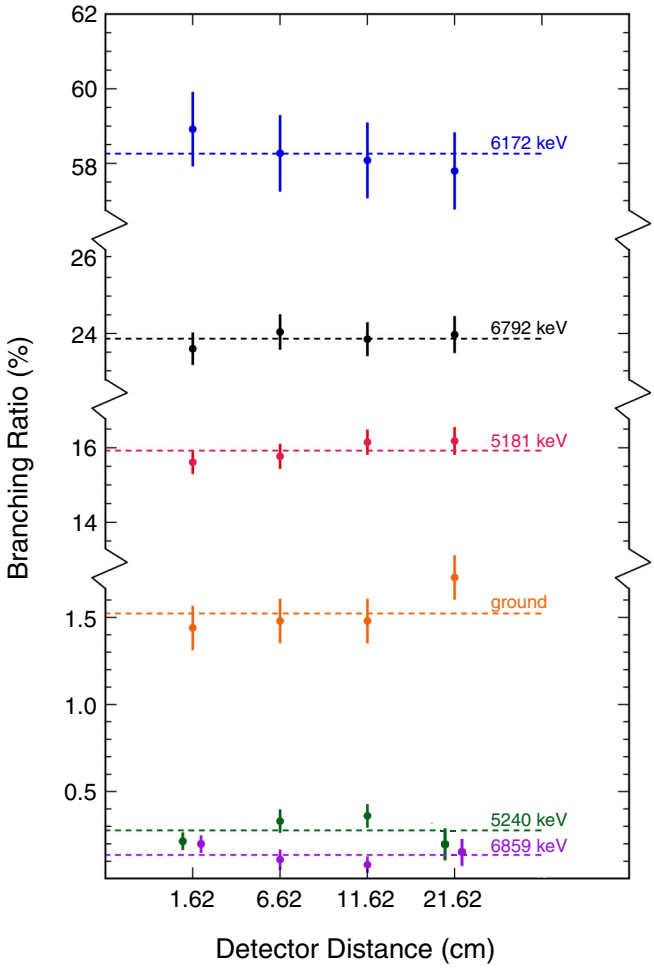

FIG. 8. Branching ratios measured using the HPGe detector at distances of 1.62, 6.62, 11.62, and 21.62 cm from the target to the detector crystal. The dashed lines are the weighted averages of the individual measurements for each transition, which are listed in Table III.

branching ratio was determined from the ratio

$$B(R \rightarrow E_j) = N_j^{\text{data}} \Big/ \sum_{j=1}^{m} N_j^{\text{data}}, \tag{4}$$

where N_j^{data} is the total number of events produced in the target for cascade j and m is the total number of primary branches in the decay. The total number of events in a cascade is given by

$$N_j^{\text{data}} = \frac{A_{\text{total}}^{\text{data}}}{A_j^{\text{sim}}} F_j N_j^{\text{sim}}, \tag{5}$$

where $A_{\text{total}}^{\text{data}}$ is the total number of detected counts, and A_j^{sim} is the total number of simulated counts associated with cascade j. The quantity N_j^{sim} is the total number of simulated events for cascade j, and F_j is the fraction of $A_{\text{total}}^{\text{data}}$ corresponding to this cascade. The simulated total efficiency is then $A_j^{\text{sim}}/N_j^{\text{sim}}$. Note that no summing corrections were necessary since the GEANT4 simulations automatically modeled coincidence summing. In addition, since the fits also include the Compton events, which make up the majority of events in the spectrum, this technique is inherently more sensitive to weak transitions, such as the ground-state transition.

TABLE III. Summary of branching ratios (%).

Transition $R \rightarrow$	Ref. [2]	Ref. [3]	Ref. [6]	HPGe[a]	APEX	Adopted[b]
0	1.70(7)	1.6(1)	1.49(4)	1.52(9)	1.49(3)	1.50(3)[c]
5181	17.3(2)	17.1(2)	17.3(2)	15.92(21)	16.25(17)	16.9(4)
5240		0.6(3)	0.15(3)	0.28(5)		0.22(7)[d]
6172	58.3(5)	57.8(3)	58.3(4)	58.26(54)	58.98(20)	58.3(3)
6792	22.7(3)	22.9(3)	22.6(3)	23.86(24)	23.28(28)	23.0(3)
6859				0.14(4)		0.14(4)

[a]Weighted average of branching ratios measured independently at detector distances of 1.62, 6.62, 11.62, and 21.62 cm from the target to the detector crystal.
[b]Weighted average of present results and Ref. [2,3,6] except where noted.
[c]Weighted average of present results and Ref. [6].
[d]Simple average of present results and Ref. [6].

The 1.62-cm spectrum and fit are shown in Fig. 7. In this case we find that a 2σ range in the residuals contains somewhat more than 95% of the data. In other words deviations between the fit and the data are consistent with the statistics of the data, which is also the case for the fits at the other detector distances. Thus, we conclude that the fits are good representations of the data. The branching ratios extracted from each spectrum are displayed in Fig. 8. These branching ratios are combined in a weighted average in Table III. It should be noted that the branching ratios for the strong transitions agree within uncertainties for each detector distance, while the ground-state transition at 20 cm is marginally in disagreement (at the 1σ level) with what is extracted at the other three distances. The reason for this is unclear, but does not appear to arise from correlations amongst the different templates. Therefore, we have included this value in Table III. The uncertainties quoted combine the statistical uncertainties in the data, the statistical and systematic uncertainties in the GEANT4 templates, and the uncertainties associated with the fraction fits. The latter was the dominant contributor to the total uncertainty. Finally, note that we also see tentative evidence for a very weak transition to the 6859-keV state that was listed as an upper limit in Ref. [17], but not observed in more recent studies [2,3,6].

2. *APEX measurements*

Reconstructed energy spectra of γ-rays from the decay of the 259-keV resonance are shown in Fig. 9. The data have been sorted based on whether only one detector bar had measurable energy deposition (multiplicity 1) or whether any pair of bars have fired (multiplicity 2). The former condition accentuates the ground-state transition and thus this spectrum was used to extract branching ratios. As is apparent in Fig. 9, the resolution of the APEX detector makes it difficult to determine peak intensities through traditional means. Consequently, the multiplicity-1 spectrum was analyzed using the

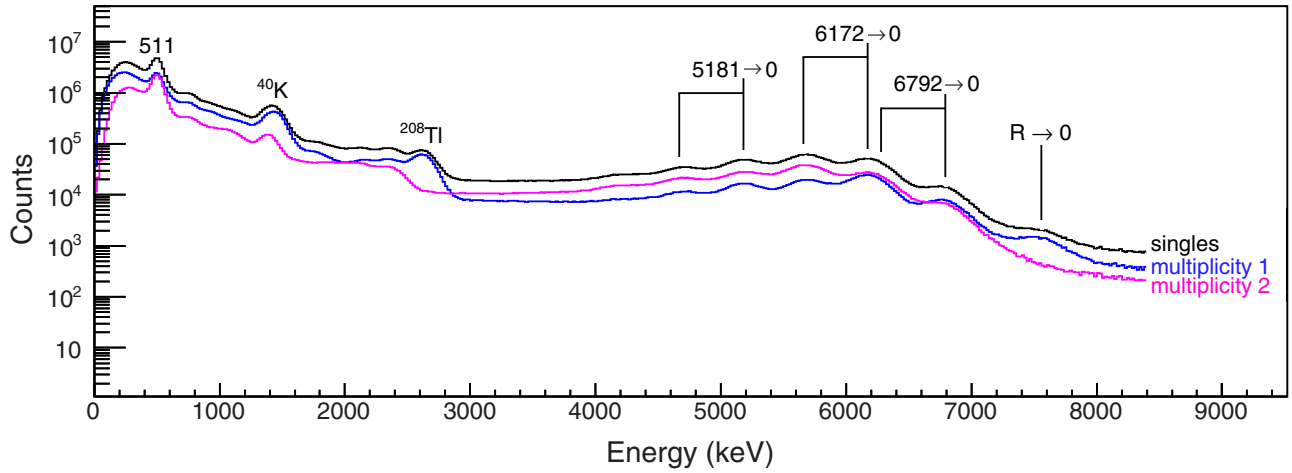

FIG. 9. Reconstructed APEX energy spectra of γ rays from the decay of the 259-keV resonance with imposed multiplicity-1 and -2 cuts. The ground-state and secondary γ rays for transitions to the 5181-, 6172-, and 6792-keV states are indicated as well as their corresponding single-escape peaks.

template-fitting procedure discussed above and in Refs. [48,49]. The resulting fit, covering an energy range of 3–8 MeV is shown in Fig. 10. Note that there was no evidence for the weak branches to the 5240- and 6859-keV states in the APEX data, which points to a disadvantage of the APEX detector. Although the relatively high efficiency meant that the statistical uncertainties in the branching ratios were negligible, the poor resolution meant that a possible 5420-keV transition could not be distinguished from much stronger 5181-keV transition. In contrast, the HPGe spectrum had fewer counts and so statistical uncertainties contributed to the branching ratios. On the other hand, the weak transitions could be distinguished because of the high resolving power of the HPGe detector. Again, no summing corrections were necessary since the GEANT4 simulations automatically modeled coincidence summing. Because of the granularity of the APEX detector, this was a negligible effect for the strong transitions, but still amounted to about 27% of the observed yield of the ground-state transition. The branching ratios determined from these and previous measurements are summarized in Table III. Our adopted branching ratio for the $R \rightarrow 0$ transition does not include those of Refs. [2,3] because of residual coincidence summing in both results. However, the effect of summing on the stronger transitions in these measurements was indeed negligible and thus Refs. [2,3] are included for the stronger transitions. In general, there is good agreement amongst these data sets for the four strongest transitions. However, the current branching ratios for the $R \rightarrow$ 5181-keV and $R \rightarrow$ 6792-keV transitions are somewhat lower and higher, respectively, than the values reported by Refs. [2,3,6] and this is particularly true of the $R \rightarrow$ 5181-keV branching ratio measured with the HPGe detector. If this result were excluded from the average, then our recommended branching ratio would change from 16.9(4)% to 17.0(3)%, which is not statistically significant. The increased uncertainty in our adopted value of 16.9(4)% versus those of the previous results is indicative of the spread in these measurements.

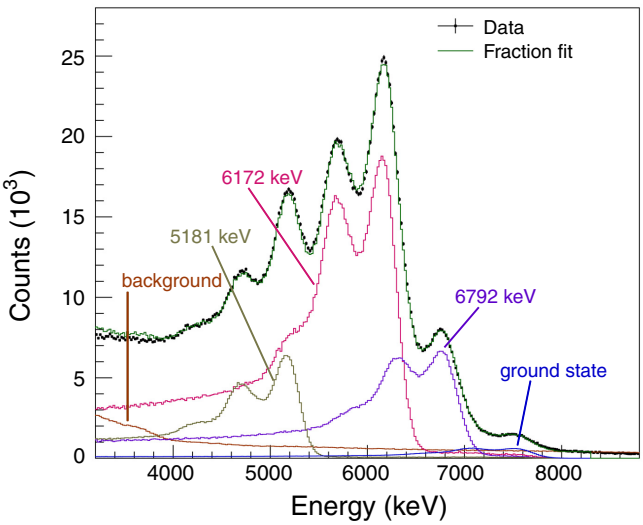

FIG. 10. Maximum-likelihood fit of the multiplicity-1 data collected with the APEX detector. The data are denoted by the black points, the fit by the green line and the individual templates are displayed as the colored histograms.

C. Resonance strength

We have determined the strength of the 259-keV resonance by measuring the γ-ray yield as a function of energy and also from the total yields of the spectra used to extract branching ratios. The former technique, while straightforward, requires the branching ratios determined in Sec. III B and the calculation of summing corrections. In contrast, the latter approach is more self-consistent in the sense that the template-fitting used to determine the branching ratios also yields the total number of reactions, which is proportional to the resonance strength.

1. Analysis of yield curves

For an infinitely-thick target, the resonance strength, $\omega\gamma$ can be related to measured yield at the maximum of the excitation function, $Y_{\text{max},\infty}$ via [51]

$$\omega\gamma = \frac{2\epsilon_{\text{eff}}}{\lambda_r^2} Y_{\text{max},\infty}, \tag{6}$$

where λ_r^2 is the de Broglie wavelength and ϵ_{eff} is the effective stopping power at the resonance energy, which for our targets can be expressed as

$$\epsilon_{\text{eff}} = \epsilon_r(\text{N}) + \frac{N_{\text{Ta}}}{N_{\text{N}}}\epsilon_r(\text{Ta}). \tag{7}$$

Here, $\epsilon_r(\text{N})$ and $\epsilon_r(\text{Ta})$ are the stopping powers for nitrogen and tantalum, respectively, evaluated at the resonance energy and $N_{\text{Ta}}/N_{\text{N}}$ is the ratio of tantalum to nitrogen in the target, which we measure as 0.667(21). These quantities are assumed to be constant over the width of the resonance. This expression for $\omega\gamma$ must then be corrected for the finite thickness of the target. However, given that our targets have varying stoichiometry, ϵ_{eff} is not constant. Therefore, it is better to express the resonance strength in terms of the area under the yield curve, A_Y (corrected for detection efficiency) and the energy width of the target, ΔE:

$$\omega\gamma = \frac{2\epsilon_{\text{eff}}}{\lambda_r^2}\frac{A_Y}{\Delta E}, \tag{8}$$

which is shown [52] to hold for targets with varying stoichiometry and thickness.

We have measured the combined yields for the three dominant transitions, $R \rightarrow 5181$ keV, $R \rightarrow 6172$ keV, and $R \rightarrow 6792$ keV, for 23 different targets. Together, these transitions account for 98.2% of the total decay strength. The measured yields were corrected for coincidence summing [51], which also included a small correction for the angular correlation between primary and secondary γ rays. The yield curve for each target was then fit using an expression for the yield from a target of finite thickness, with corrections for beam-energy spread and energy straggling. The yield, target width, energy width, and energy straggling were independently varied using a Markov chain Monte Carlo [53] to produce a fit to the experimental data. Finally, the theoretical curve was integrated to extract A_Y. An example of an experimental yield curve and fit are shown in Fig. 11 and the resonance strengths determined from each target are shown in Fig. 12.

The uncertainties in the strengths and weighted average shown in Fig. 12 are statistical. However, the dominant source of uncertainty is systematic and arises from beam-current integration (2.5%), resonance energy (0.077%), the total branching ratio for the 3 measured transitions (0.1%), and ϵ_{eff} (3.6%). The stopping powers in ϵ_{eff} were calculated with SRIM-2013 [20] and we estimate that $\epsilon_r(\text{N})$ and $\epsilon_r(\text{Ta})$ represent the available stopping-power data to about 3% and 5%, respectively. We have also calculated stopping powers using the codes CASP (version 5.2) [54] (using the UCN model and the charge-state scan screening function) and PSTAR [55]. The effective stopping powers from SRIM and CASP agree within 5%, which is approximately consistent with our assigned uncertainty of 3.6%. The PSTAR stopping power for nitrogen agrees with SRIM within our assumed uncertainty and although there is agreement between PSTAR and SRIM for tungsten, the PSTAR database does not include tantalum. Therefore, we have adopted stopping powers from SRIM for the purpose of this study. After including systematic uncertainties, our resonance strength is $\omega\gamma_{259} = 12.60 \pm 0.15(\text{stat}) \pm 0.55(\text{sys})$ meV.

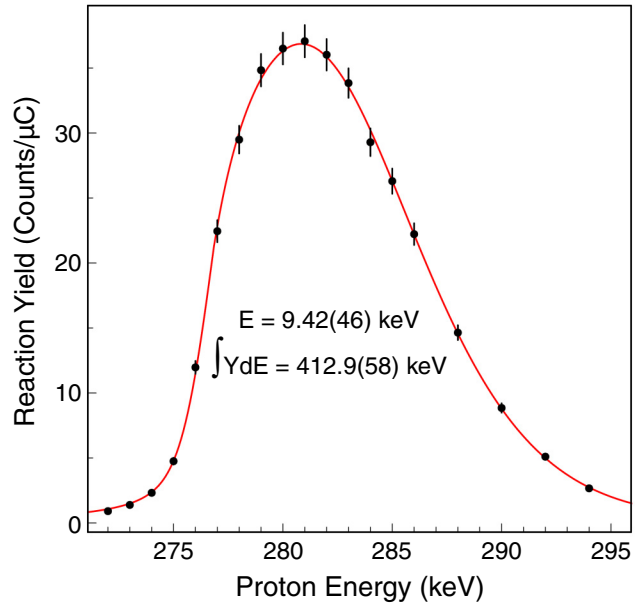

FIG. 11. An example of a yield curve for the 259-keV resonance. The Markov chain Monte Carlo fit is denoted by the red line.

2. Fraction fit of HPGe and APEX spectra

The fraction-fit procedure yields N_j^{data}, the total number of events produced in the target for cascade j. The sum over all cascades is thus a measure of the total yield of the reaction,

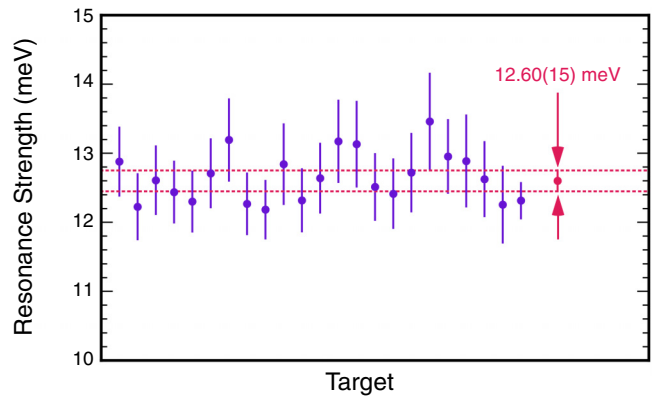

FIG. 12. Resonance strengths extracted from independent yield-curve measurements on 23 separate targets (blue points). The red point and dashed lines represent the weighted average of the individual points. Note that only statistical uncertainties are shown.

TABLE IV. Summary of resonance strengths (in meV), including estimated statistical and systematic and total uncertainties.

Measurement	$\omega\gamma_{259}$ (meV)	Stat.	Sys.	Total
Becker *et al.* [19]	13.7			1.0
Runkle *et al.* [2]	12.4	0.4	0.8	0.9
Imbriani *et al.* [3]	12.9	0.4	0.8	0.9
Bemmerer *et al.* [5]	12.8	0.3	0.5	0.6
Yield curves	12.60	0.15	0.55	0.6
HPGe fraction fit	12.42	0.29	0.55	0.6
APEX fraction fit	12.76	0.20	0.57	0.6
Recommended[a]	12.6			0.3

[a]Weighted average of present results and Refs. [2,3,5], as described in the text.

which is related to the quantity $Y_{\max,\infty}$ in Eq. (6) via

$$Y_{\max,\infty} = \frac{A_Y}{\Delta E}\sum_{j=1}^{m} N_j^{\text{data}}, \tag{9}$$

which corrects for nonuniform stoichiometry and finite target width. As described above, A_Y is the area under the yield curve and ΔE is the energy width. The difference between this approach and the analysis of yield curves above is that the correction factor $A_Y/\Delta E$ is applied to the raw spectrum and thus there are no corrections for summing, which is accounted for when the templates are constructed. The resulting resonance strengths are $\omega\gamma_{259} = 12.42 \pm 0.29(\text{stat}) \pm 0.55(\text{sys})$ meV (HPGe) and $\omega\gamma_{259} = 12.76 \pm 0.20(\text{stat}) \pm 0.57(\text{sys})$ meV (APEX). The latter was derived from both the multiplicity-1 and multiplicity-2 data shown in Fig. 9. The statistical uncertainties quoted here arise primarily from the statistics of the experimental spectra and the fraction fits (which includes an uncertainty of 3% in the calculated efficiency, $A_j^{\text{sim}}/N_j^{\text{sim}}$). The systematic uncertainties are identical to what was used in the analysis of yield curves. The results of the current measurements are summarized in Table IV.

IV. DISCUSSION

In Table IV we list present and previous measurements of $\omega\gamma_{259}$. The latter have been reevaluated as needed, as described in the Appendix. Overall, there is excellent agreement within estimated uncertainties. Our recommended value is $\omega\gamma_{259} = 12.6(3)$ meV, which is in agreement with 13.1(6) meV from Ref [18], but is more precise. This was obtained via a weighted average of the present results and those of Refs. [2,3,5] and does not include that of Becker *et al.* [19]. While it is true that Peirce's criterion [29] would identify this result as an outlier, we instead exclude it because of the lack of measured stopping powers, as discussed in more detail in the Appendix. If this value were included, then our recommended strength would increase to $\omega\gamma_{259} = 12.7(3)$.

The measurements using Ta_2N_3 targets (the present measurements and that of Ref. [2]) share a common systematic uncertainty associated with ϵ_{eff}, primarily from the Ta/N ratio. Consequently, we first took a weighted average of the these results without including the uncertainty in ϵ_{eff} in the systematic uncertainties. This common uncertainty was then added to the overall uncertainty before the Ta_2N_3 measurements were averaged with the other results. This procedure differed from that employed in Ref. [18] in which a common systematic uncertainty associated with the stopping power of protons in nitrogen was removed before taking the average. This is because the uncertainties in the effective stopping powers for the TiN and Ta_2N_3 targets are dominated by the Ti/N and Ta/N ratios, respectively whereas for the H_2 target, $\epsilon_{\text{eff}} = \epsilon_r(\text{N})$. In other words, from a numerical standpoint, the systematic uncertainty associated with target composition is independent for the three targets used in these measurements. However, it turns out that there is essentially no difference between the average calculated in this way and a simple weighted average of all of the entries in Table IV. Finally, note that since all of the uncertainties quoted in Table IV are dominated by systematic uncertainties that are largely estimated, we have calculated the weighted average using the bootstrapping technique mentioned earlier, which provides a more reliable estimate of the overall uncertainty than an average of weights.

The strengths listed in Table IV are all based on stopping powers calculated using SRIM. With the exception of those used in the measurement by Becker *et al.* [19], there are experimental data strongly suggesting that these stopping powers are reliable. As mentioned above, the major source of uncertainty in ϵ_{eff} for the solid targets is the Ta/N or Ti/N ratio. While these also depend on stopping powers (for 2-MeV α particles used in RBS measurements), the primary limitation on the precision of the measured stochiometries is that RBS is more sensitive at measuring the concentration of a heavy nucleus in a lighter substrate than for the reverse situation, which is the case for both the Ta_2N_3 and TiN targets. On the other hand, improved measurements of the stopping power of protons in nitrogen would directly reduce the systematic uncertainties in measurements made using H_2 targets. Finally, we note that stopping powers calculated using CASP are also in agreement with data for protons, but are somewhat lower than SRIM stopping powers. While it is true that CASP does not include nuclear stopping, this is only a small part of the total stopping power [e.g., 0.09% of ϵ(N)] and does not account for the difference with respect to SRIM. The CASP stopping powers for helium in N, Ti, and Ta, which determine the stochiometries of the solid targets, are substantially lower than measured values. Thus, it appears that SRIM does the best job overall of reproducing all of the experimental data that are relevant here.

V. CONCLUSION

We have measured excitation energies and branching ratios for states populated in the decay of the 259-keV resonance in $^{14}\text{N}(p,\gamma)^{15}\text{O}$. Our recommended resonance strength is $\omega\gamma_{259} = 12.6(3)$ meV, which is in agreement with 13.1(6) meV from Ref. [18], but is more precise. Using this result, the previous S-factor data of Runkle *et al.* [2] should be reduced by 6.7%, those of Imbriani *et al.* [3] by 2.3% and Marta *et al.* [6] by 3.8%. As a consequence, these measurements are now closer in accord with the gas-target result [5]. While new R-matrix

calculations are beyond the scope of this paper, the uncertainty in the overall normalization of the S factors is reduced from 4.6% to 2.4%. In addition, given the previous R-matrix fits [18], the S factor at zero energy for the $^{14}\mathrm{N}(p,\gamma)^{15}\mathrm{O}$ reaction should be reduced from 1.66(12) to 1.60(9) keV b. This uncertainty includes the ±0.08 keV b uncertainty estimated in Ref. [18] in the R-matrix fits, which is now the dominant source of uncertainty in extrapolations of $S(0)$.

ACKNOWLEDGMENTS

This work was supported in part by the US Department of Energy under Contract No. DE-FG02-97ER41041 and by the U.S. Department of Energy National Nuclear Security Administration under Contract No. DE-FC52-08NA28752. We would like to thank J. R. Dermigny for his assistance with the fraction fits.

APPENDIX: REVIEW OF PREVIOUS RESULTS

As mentioned in the Introduction, the recommended resonance strength of Adelberger *et al.* [18] combined some previous results that assumed different branching ratios than what are recommended here as well as stopping powers that may require revision. Here we review the previous measurements and recommend new resonance strengths where appropriate. In keeping with Ref. [18], we have not considered measurements performed previously to Becker *et al.* [19] (see, e.g., Ref. [56] and references therein). This is primarily because the stopping powers that were used to determine target composition and the strengths of standard resonances were based on very sparse experimental information and little guidance is given that would allow us to correct for these stopping powers or to estimate statistical and systematic uncertainties. For consistency, our recommended resonance strengths use stopping powers calculated using the 2013 version of SRIM [20], but we also consider the results obtained using other codes.

Becker *et al.* [19] report a strength $\omega\gamma_{259} = 14(1)$ meV, based on measurements relative to the 324-keV resonance in the $^{19}\mathrm{F}(p,\alpha_2\gamma)^{16}\mathrm{O}$ reaction. Both measurements were carried out in inverse kinematics using a hydrogen-gas target. The $R \rightarrow 6792$ transition was used to determine the yield with an assumed branching ratio of 23.3(6)% [57], which agrees within uncertainties with our recommended value of 23.0(3)%. The strength of the reference resonance was measured relative to Rutherford scattering and therefore does not require knowledge of stopping powers. On the other hand, $\omega\gamma_{259}$ was obtained from the relative relationship between yields and resonance strengths [51] and does depend on stopping powers:

$$\omega\gamma_1 = \omega\gamma_2 \frac{Y^1_{\mathrm{max},\infty}}{Y^2_{\mathrm{max},\infty}} \frac{E_1}{E_2} \frac{\epsilon_1}{\epsilon_2}, \tag{A1}$$

where in this case subscript/superscript 1 refers to the 259-keV resonance and subscript/superscript 2 refers to the reference resonance. The measured yield must be corrected for finite target thickness via a factor $\tan^{-1}(\Delta E/\Gamma)$, where ΔE is the thickness of the target (approximately 7.64 keV in the center-of-mass frame) and Γ is the total width of the 259-keV resonance, taken to be $\Gamma_{\mathrm{c.m.}} = 1.2(2)$ keV by Becker *et al.* A weighted average of more recent measurements [3,7,44] is $\Gamma_{\mathrm{c.m.}} = 0.999(46)$ keV.

The ratio of stopping powers was originally obtained from the tables of Northcliffe and Schilling [21] and unfortunately, there is little experimental information on which to base these calculations. Apparently, only one measurement exists for $^{14}\mathrm{N} + \mathrm{H}_2$ at the energy of interest [58] and there are no measurements for $^{19}\mathrm{F} + \mathrm{H}_2$. We have compared the Northcliffe and Schilling stopping powers with those calculated using SRIM, CASP, and MSTAR (version 3.12) [59] and find $\epsilon_r(\mathrm{N}+\mathrm{H})/\epsilon_r(\mathrm{F}+\mathrm{H}) = 0.686$ (Northcliffe and Schilling), 0.689 (SRIM), 0.839 (CASP), and 0.901 (MSTAR). The values for $\epsilon_r(\mathrm{N}+\mathrm{H})$ from Northcliffe and Schilling, SRIM, and MSTAR are consistent with the measured value within its ±15% uncertainty whereas CASP predicts a value that is lower by about 27%. On the other hand, the $\epsilon_r(\mathrm{F}+\mathrm{H})$ values from Northcliffe and Schilling, SRIM, and CASP span a range of 5.4%, but that from MSTAR is 32% below the average of these three values. Given the paucity of experimental information, it is difficult to determine which data set to use for the ratio of stopping powers.

Assuming the new values for the branching ratio and Γ, we obtain $\omega\gamma_{259} = 13.6(10)$ meV using stopping powers from Northcliffe and Schilling. Here we have simply kept the same percent uncertainty as in the original result. Similarly, we obtain $\omega\gamma_{259} = 13.7(10), 16.7(12)$, and 17.9(13) meV using stopping powers from SRIM, CASP, and MSTAR, respectively. Only the strengths calculated with Northcliffe and Schilling or SRIM stopping powers are consistent with our new measurements or the others that we will describe below and thus we recommend the value obtained using SRIM stopping powers, $\omega\gamma_{259} = 13.7(10)$ meV.

Runkle *et al.* [2] measured the yield of the $R \rightarrow 6172$ transition and used Eq. (6) to extract $\omega\gamma_{259} = 13.5(12)$ meV. Small corrections should be made to reflect the branching ratio for this transition as listed in Table III as well as the effect of nonuniform stoichiometry in their implanted nitrogen target on $Y_{\mathrm{max},\infty}$. This latter correction (∼0.5%) involved the use of Eq. (8) to determine the resonance strength. We have also revised the detection efficiencies using our GEANT4 simulations. The biggest change that we find is in target stoichiomentry, which affects ϵ_{eff}. The targets used by Runkle *et al.* were nitrogen implanted into tantalum, prepared in an identical manner to the targets used in this study. Their stoichiometry, Ta/N = 0.718(25) was determined as in this study, by comparing RBS yields for nitrogen-implanted tantaulm and pure tantaulum. However, they used the ratio of plateau heights (i.e., Eq. (1) from Ref. [28]) to measure the stoichiometry, which is based on the assumption that the stopping power is nearly constant over the width of the implanted region. Our RBS analyses indicate that the nitrogen concentration, and thus the stopping power, does vary and consequently we have used our current value of Ta/N = 0.667(21). Taken together, these corrections lower the resonance strength of Runkle *et al.* from 13.5(12) meV to $12.4 \pm 0.4(\mathrm{stat}) \pm 0.8(\mathrm{sys})$ meV.

Imbriani *et al.* [3] measured $\omega\gamma_{259} = 12.9 \pm 0.4(\mathrm{stat}) \pm 0.8(\mathrm{sys})$ meV using a TiN target. However, it is not clear

which transition was measured and thus it is also not clear if corrections for branching ratios are warranted. On the other hand, these corrections would be very small. The stopping powers used are from SRIM and have not changed in subsequent releases. As result, we adopt thus resonance strength as published.

Finally, $\omega\gamma_{259} = 12.8 \pm 0.3(\text{stat}) \pm 0.5(\text{sys})$ meV was reported by Bemmerer *et al.* [5] using an H_2 gas target. Since they measured the total yield using a summing detector, there is no dependence on branching ratios. Again SRIM stopping powers were used and consequently we adopt the published resonance strength.

[1] A. Formicola, G. Imbriani, H. Costantini, C. Angulo, D. Bemmerer, R. Bonetti, C. Broggini, P. Corvisiero, J. Cruz, P. Descouvemont *et al.*, Phys. Lett. B **591**, 61 (2004).

[2] R. C. Runkle, A. E. Champagne, C. Angulo, C. Fox, C. Iliadis, R. Longland, and J. Pollanen, Phys. Rev. Lett. **94**, 082503 (2005).

[3] G. Imbriani, H. Costantini, A. Formicola, A. Vomiero, C. Angulo, D. Bemmerer, R. Bonetti, C. Broggini, F. Confortola, and P. Corvisieros, Eur. Phys. J. A **25**, 455 (2005).

[4] A. Lemut, D. Bemmerer, F. Confortola, R. Bonetti, C. Broggini, P. Corvisiero, H. Costantini, J. Cruz, A. Formicola, Z. Fülöp *et al.*, Phys. Lett. B **634**, 483 (2006).

[5] D. Bemmerer, F. Confortola, A. Lemut, R. Bonetti, C. Broggini, P. Corvisiero, H. Costantini, J. Cruz, A. Formicola, Z. Fülöp *et al.*, Nucl. Phys. A **779**, 297 (2006).

[6] M. Marta, A. Formicola, G. Gyürky, D. Bemmerer, C. Broggini, A. Caciolli, P. Corvisiero, H. Costantini, Z. Elekes, Z. Fülöp *et al.*, Phys. Rev. C **78**, 022802(R) (2008).

[7] U. Schröder, H. Becker, G. Bogaert, J. Görres, C. Rolfs, H. Trautvetter, R. Azuma, C. Campbell, J. King, and J. Vise, Nucl. Phys. A **467**, 240 (1987).

[8] S. Degl'Innocenti, G. Fiorentini, B. Ricci, and F. Villante, Phys. Lett. B **590**, 13 (2004).

[9] J. Bahcall, A. Serenelli, and S. Basu, Astrophys. J. **621**, L85 (2005).

[10] Y. Kishimoto *et al.* (KamLAND Collaboration), J. Phys. Conf. Ser. **120**, 052010 (2008).

[11] R. S. Raghavan *et al.* (LENS Collaboration), J. Phys. Conf. Ser. **120**, 052014 (2008).

[12] S. Capelli *et al.* (CUORICINO Collaboration), Nucl. Phys. B (Proc. Suppl.) **221**, 334 (2011).

[13] F. Villante, A. Ianni, F. Lombardi, G. Pagliaroli, and F. Vissani, J. Phys. Conf. Ser. **375**, 042035 (2012).

[14] V. Lozza *et al.* (Sno+ Collaboration), J. Phys. Conf. Ser. **375**, 042050 (2012).

[15] M. Wurm, D. Bick, T. Enqvist, D. Hellgartner, M. Kaiser, K. K. Loo, S. Lorenz, M. Meloni, M. Meyer, R. Möllenber *et al.*, Physics Procedia **61**, 376 (2015).

[16] W. Haxton and A. Serenelli, Astrophys. J. **687**, 678 (2008).

[17] F. Ajzenberg-Selove, Nucl. Phys. A **523**, 1 (1991).

[18] E. Adelberger, A. García, R. G. H. Robertson, K. A. Snover, A. B. Balantekin, K. Heeger, M. J. Ramsey-Musolf, D. Bemmerer, A. Junghans, C. A. Bertulani *et al.*, Rev. Mod. Phys. **83**, 195 (2011).

[19] H. W. Becker, W. E. Kieser, C. Rolfs, H. P. Trautvetter, and M. Wiescher, Z. Phys. A **305**, 319 (1982).

[20] J. F. Ziegler and J. P. Biersack, computer program SRIM, version 2013 (2013).

[21] L. Northcliff and R. Schilling, Nucl. Data **7**, 233 (1970).

[22] S. V. Artemov, S. B. Igamo, Q. I. Tursunmakhatov, and R. Yarmukhamedov, Phys. At. Nucl. **75**, 291 (2012).

[23] J. Grineviciute and D. Halderson, J. Phys. G **35**, 055201 (2008).

[24] R. J. de Boer, D. W. Bardayan, J. Görres, P. J. LeBlanc, K. V. Manukyan, M. T. Moran, K. Smith, W. Tan, E. Uberseder, M. Wiescher *et al.*, Phys. Rev. C **91**, 045804 (2015).

[25] D. Vermilyea, Acta Metall. **1**, 282 (1953).

[26] P. Attayek, E. Meyer, L. Lina, G. Rich, T. Clegg, and O. Coronell, Nucl. Instrum. Methods A **676**, 21 (2012).

[27] M. Mayer, computer program SIMNRA (2011).

[28] J. Keinonen and A. Antilla, Nucl. Instrum. Methods. **160**, 211 (1979).

[29] B. Peirce, Astron. J. **2**, 161 (1852).

[30] B. Efron and R. Tibshirani, Stat. Sci. **1**, 54 (1986).

[31] M. Birch, Visual Averaging Library, available from http://www.nndc.bnl.gov/nndcscr/ensdf_pgm/utility/vavglib/ (2014).

[32] N. I. Kaloskamis, K. C. Chan, A. A. Chishti, J. S. Greenberg *et al.*, Nucl. Instrum. Methods A **330**, 447 (1993).

[33] R. R. Betts, Nucl. Instrum. Methods B **43**, 294 (1989).

[34] S. Carson, C. Iliadis, J. Cesaratto, A. Champagne, L. Downen, M. Ivanovic, J. Kelley, R. Longland, J. Newton, G. Rusev, and A. Tonchev, Nucl. Instrum. Methods A **618**, 190 (2010).

[35] R. Longland, C. Iliadis, A. E. Champagne, C. Fox, and J. R. Newton, Nucl. Instrum. Methods. A **566**, 452 (2006).

[36] I. J. Kim, C. S. Park, and H. D. Choi, Appl. Radiat. Isotopes **58**, 227 (2003).

[37] S. Agostinelli *et al.*, Nucl. Instrum. Methods. A **506**, 250 (2003).

[38] C. Howard, C. Iliadis, and A. Champagne, Nucl. Instrum. Methods A **729**, 254 (2013).

[39] D. Radford, RADWARE, available from http://radware.phy.ornl.gov/ (2011).

[40] P. F. Bertone, A. E. Champagne, D. C. Powell, C. Iliadis, S. E. Hale, and V. Y. Hansper, Phys. Rev. Lett. **87**, 152501 (2001).

[41] D. Schürmann, R. Kunz, I. Lingner, C. Rolfs, F. Schümann, F. Strieder, and H.-P. Trautvetter, Phys. Rev. C **77**, 055803 (2008).

[42] K. Yamada, T. Motobayashi, H. Akiyoshi, N. Aoi, Zs. Fülöp, T. Gomi, Y. Higurashi, N. Imai, N. Iwasa, H. Iwasaki *et al.*, Phys. Lett. B **579**, 265 (2004).

[43] N. Galinski, S. K. L. Sjue, G. C. Ball, D. S. Cross, B. Davids, H. A. Falou, A. B. Garnsworthy, G. Hackman, U. Hager, D. A. Howell *et al.*, Phys. Rev. C **90**, 035803 (2014).

[44] M. Borowski, K. P. Lieb, M. Uhrmacher, and W. Bolse, *Capture Gamma-Ray Spectroscopy and Related Topics*, Proceedings of the 13th International Symposium on Capture Gamma-Ray Spectroscopy and Related Topics August 2008, Cologne (Germany), edited by J. Jolie, A. Zilges, N. Warr, and A. Blazhev, AIP Conf. Proc. No. 1090 (AIP, New York, 2009), p. 450.

[45] M. Wang, G. Audi, A. Wapstra, F. Kondev, M. MacCormick, X. Xu, and B. Pfeiffer, Chin. Phys. C **36**, 1603 (2012).

[46] R. Barlow and C. Beeston, Comput. Phys. Commun. **77**, 219 (1993).
[47] R. Brun and F. Rademakers, Nucl. Instrum. Methods A **389**, 81 (1997).
[48] M. Q. Buckner, C. Iliadis, K. J. Kelly, L. N. Downen, A. E. Champagne, J. M. Cesaratto, C. Howard, and R. Longland, Phys. Rev. C **91**, 015812 (2015).
[49] K. J. Kelly, A. E. Champagne, R. Longland, and M. Q. Buckner, Phys. Rev. C **92**, 035805 (2015).
[50] J. R. Dermigny, C. Iliadis, M. Q. Buckner, and K. J. Kelly, Nucl. Instrum. Methods A **830**, 427 (2016).
[51] C. Iliadis, *Nuclear Physics of Stars* (Wiley-VCH, Weinheim, 2015).
[52] D. W. Palmer, J. G. Skofronick, D. G. Costello, A. L. Morsell, W. E. Kane, and R. G. Herb, Phys. Rev. **130**, 1153 (1963).
[53] R. Longland, computer program MCMCYIELD (2013).
[54] G. Schiwietz and P. Grande, Nucl. Instrum. Methods B **273**, 1 (2012).
[55] M. Berger, J. Coursey, M. Zucker, and J. Chang, computer program PSTAR, available at http://physics.nist.gov/PhysRefData/Star/Text/PSTAR.html (2005).
[56] D. Hebbard and G. Bailey, Nucl. Phys. **49**, 666 (1963).
[57] F. Ajzenberg-Selove, Nucl. Phys. A **268**, 1 (1976).
[58] Ya. A. Teplova, V. S. Nikolaev, I. S. Dmitriev, and L. N. Fateeva, Sov. Phys. JETP **15**, 31 (1962).
[59] H. Paul and A. Schinner, Nucl. Instrum. Methods B **179**, 299 (2001).